ELSEVIER

PII: S0309-1708(98)00047-5

Advances in Water Resources Vol. 22, No. 7, pp 681–696, 1999

0309-1708/99/$ – see front matter

Adaptive-grid simulation of groundwater flow in heterogeneous aquifers

Jun Cao* **& Peter K. Kitanidis**

Civil and Environmental Engineering, Stanford University, Stanford, CA 94305-4020, USA

(Received 4 May 1998; accepted 14 November 1998)

The prediction of contaminant transport in porous media requires the computation of the flow velocity. This work presents a methodology for high-accuracy computation of flow in a heterogeneous isotropic formation, employing a dual-flow formulation and adaptive gridding. The dual equations, describing the hydraulic head and the streamfunction, are numerically solved through finite element approximations. The application of classic finite-element methods requires a rather large number of nodes to represent suitably the flow in high-contrast formations. We present a mesh-adaptive approach that enhances the accuracy of the numerical flow solution for a given computational effort. We rely on an *a posteriori* error estimator to identify areas where refinements of the finite element mesh are needed or unrefinements are acceptable. We also demonstrate through numerical experiments that the developed methodology efficiently enhances accuracy through successive mesh adaptation. © 1999 Elsevier Science Ltd. All rights reserved

1 INTRODUCTION

Numerical simulation models are routinely used in hydrogeologic investigations. Many of these models employ finite-element approximations, which are flexible in describing complicated geometries and intricate physical phenomena. Finite element methods have been frequently applied to solve groundwater flow and transport problems[1–10].

One of the challenges of quantitative hydrogeology is the modelling of single-phase fully saturated flow in highly heterogeneous formations. The flow in such formations tends to channel into preferential flow paths[11,12] and, in the case of very large conductivity variation, the flow regime resembles a network[13]. The error associated with numerical simulation of such flows using coarse grids has been shown to be quite significant[3,12]. The finer the grid, the smaller the truncation error and, to prevent numerical dispersion, the grid size should be about the inverse of the gradient of the logarithm of transmissivity[14].

When using finite element methods, the hydraulic potential, ϕ, is usually first computed; then, the velocity is calculated through application of Darcy's law and the streamlines are drawn through tracing of flow particles. It was demonstrated by Frind and Matanga[3] that such a procedure is error prone, because the streamlines are computed with lower accuracy than the equipotentials (lines of constant hydraulic head). Also, it is physically required that fluxes across element edges should be conforming, but this physical feature cannot be guaranteed with the application of Darcy's law, which leads to a constant velocity for each element when linear finite elements are employed. On this topic, some mixed finite element methods or mixed-hybrid finite element methods have been proposed[15,7,16–18]. Frind and Matanga[3] presented a "dual flow" formulation in the study of groundwater flow in heterogeneous aquifers. That is, the hydraulic head and the steamfunction are computed separately and with similar accuracy. This approach has been shown[19,20] to yield accurate predictions of advective transport and mixing.

The "dual flow" formulation leads to a set of two Laplace-like equations. Solving such equations is still a challenging problem especially for highly heterogeneous

* Corresponding author. Tel.: 01 604 4318236; fax: 01 604 2914947; jcao@cs.sfu.ca

media. Borcea and Papanicolaou[12] have shown that obtaining an accurate numerical solution of second-order elliptic problems with large contrast in the coefficients is not an easy task. However, an accurate description of the velocity field is a prerequisite for a realistic analysis of the advective–dispersive–reactive contaminant transport processes[21,22]. In mixing-limited reactions, the use of inaccurate velocity causes miscalculation of the rate of mixing and thus the rate of chemical reactions, as shown by Cirpka *et al.*[21]. Neglecting spatial variability may be inappropriate when heterogeneity has strong influence on mixing. Thus, one must include heterogeneity in the numerical simulation and use algorithms that are accurate enough to preserve the effects of heterogeneity. If one uses uniform finite element meshes, many nodes are required in order to capture the high-flow zones. However, the flow rate in most of the domain is slow and can be represented adequately with a lower density of nodes. Thus, using fine uniform grids results in inefficient use of computational resources.

Employing an *a posteriori* error estimator, this work extends the approach of Frind and Matanga[3] to use nonuniform adaptively selected grids, on which error is first distributed more uniformly and then the error magnitude is further globally reduced as much as needed. This new mathematical approach strikes a satisfactory balance between solution accuracy and computational efficiency. We start by obtaining the solution for a relatively coarse regular mesh; then, using a higher order approximation, we estimate the error distribution. This error distribution serves as a guide to adjust the granularity of the grid.

Mesh adaptive procedures can be classified into two broad categories. The first approach considers the existing topology as heritable; that is, local refinement/unrefinement is implemented on the basis of the previous discretization[23–25]. The other approach generates/adapts meshes relying on a certain defined metric, the previous connectivity being broken when regenerating a grid[26,27]. In our application, the higher flow rate areas are more and more clearly discovered by a series of mesh adaptations. Our procedure starts from a fairly coarse initial mesh that sequentially evolves. During the mesh evolution, we basically adopt a hierarchical-style local refinement scheme that bisects the longest edge of the triangle of interest. This method was originally proposed by Rivara [28] and is now developed by using efficient edge-swapping techniques to make mesh quality even better. Also, we incorporate into our mesh adaptive algorithm an auxiliary unrefinement tool that can delete unnecessary previously set points. An optional node-moving process can further improve the grid. Using this automated mesh adaptive procedure, the practical consequences are that high-flow areas require refinement and low-flow areas may be coarsened, depending on how much accuracy is required. Thus, the quality of the resulting flow solution is ensured while the overall processing time is significantly reduced.

This work also presents numerical simulations that illustrate the error that an inadequate grid may introduce on the computed flow regime in a heterogeneous domain. Our numerical experiments demonstrate that the *a posteriori* error estimate analysis guides the mesh adaptation algorithm to produce a high-quality grid for the accurate groundwater flow simulation in highly heterogeneous aquifers, without increasing significantly the total computational cost. The results in this study warn hydrogeologists against the use of coarse or sloppily selected grids in heterogeneous formations and provide insights that may assist practitioners in selecting a better grid.

2 MATHEMATICAL MODELING

Consider steady flow without sources or sinks throughout a square domain Ω (see Fig. 1). This flow domain and the boundary conditions are used for illustration of the methodology. Assuming that the transmissivity is isotropic, the flow equation solution can be obtained in terms of streamfunction and hydraulic potential (head), utilizing the approach known as "*dual flow*" formulation [3].

The mathematical flow model comprises two uncoupled equations: one describes ϕ, the *hydraulic head*:

$$\nabla(K\nabla\phi) = 0 \quad \text{in } \Omega \tag{1}$$

and the other describes ψ, the *streamfunction*:

$$\nabla\left(\frac{1}{K}\nabla\psi\right) = 0 \quad \text{in } \Omega, \tag{2}$$

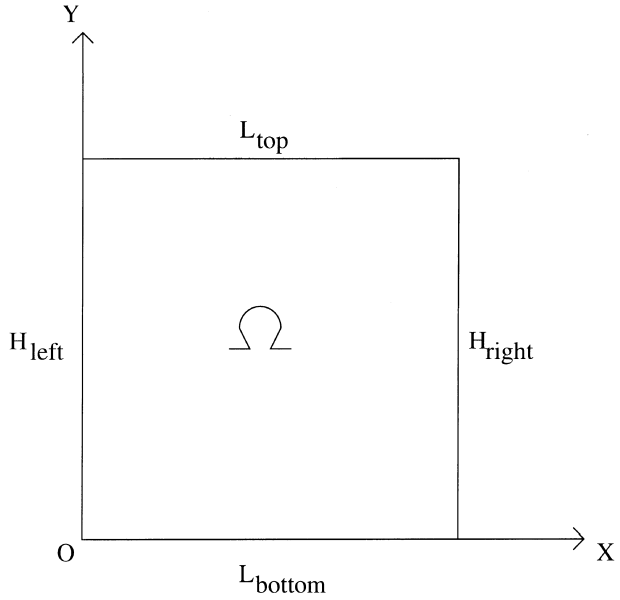

Fig. 1. Computational domain.

where K is the *hydraulic conductivity* (or *transmissivity*, for Dupuit–Forchheimer flows).

For eqn (1), use Dirichlet conditions along the left and right boundaries of the domain, L_{left} and L_{right}:

$$\phi = \phi_1 \quad \text{on } L_{\text{left}}; \quad \phi = \phi_2 \text{ on } L_{\text{right}} \tag{3}$$

and the homogeneous Neumann (no-flux) condition along top and bottom:

$$\frac{\partial \phi}{\partial n} = 0 \quad \text{on } L_{\text{top}} \cup L_{\text{bottom}}. \tag{4}$$

In eqn (4), $\partial/\partial n$ signifies the derivative along the outwards normal vector at the boundary.

The solution of the hydraulic potential problem (1), along with boundary conditions (3) and (4), provides the values of the potential at each node. Then, the Darcy flux (discharge per unit area of porous medium), which is also called "*specific discharge*", is defined as a vector function:

$$\vec{q} = (q_x, q_y)^t = \left(-K\frac{\partial \phi}{\partial x}, -K\frac{\partial \phi}{\partial y} \right)^t. \tag{5}$$

We calculate the flux across either L_{left} or L_{right} by integrating the horizontal specific discharge component along the height of the square domain:

$$\Delta\psi = \int_{\text{bottom}}^{\text{top}} q_x(y)\ \mathrm{d}y \tag{6}$$

Thus, the boundary conditions set for eqn (2) are specified as:

$$\psi = 0 \quad \text{on } L_{\text{bottom}}, \quad \psi = \Delta\psi \quad \text{on } L_{\text{top}} \tag{7}$$

and

$$\frac{\partial \psi}{\partial n} = 0 \quad L_{\text{left}} \cup L_{\text{right}}. \tag{8}$$

In the application that will be described later, to illustrate the method, the actual conductivity K is resolved at a scale smaller than that of the elements. In the implementation of the finite element method, the conductivity in each triangle τ is set uniform and equal to the geometric mean of the actual conductivity within the triangle. The geometric mean conductivity is supposed to represent the effective conductivity of an element. The problem of conductivity upscaling is reviewed in Ref.[29].

From eqn (5), the velocity can be obtained by using

$$\vec{u} = \frac{\vec{q}}{\theta} \tag{9}$$

with θ denoting the porosity of the medium. Note that one might have used eqn (9) to trace streamlines, thus obtaining a streamfunction distribution. However, the velocity is constant within each finite element, yielding only an elementwise streamfunction value distribution. This approximation does not guarantee the accuracy of streamline tracing[15,17,18]. To circumvent this obstacle, we adopt the dual flow formulation that can accurately compute both streamlines and equipotentials. We will show later in this paper that the numerical solutions in terms of equipotential lines and streamlines resulting from dual flow models are exactly orthogonal everywhere.

3 FINITE ELEMENT DISCRETIZATION

The equipotential equation (1) and the streamfunction equation (2) are similar elliptic equations. The same finite element algorithm is used to solve first eqn (1) and then eqn (2). We will use the streamfunction equation (2) to describe the method.

Define the following discrete space:

$$H_h^1 = \left\{ q_h | q_h \in C^0(\Omega), q_h|_\tau \in P_1, \forall \tau \in \Omega_h \right\}, \tag{10}$$

where Ω_h is the standard triangulation of the computational domain Ω; τ is a generic element in Ω; $C_0(\Omega)$ represents the space of functions that are continuous on Ω; $h = \max_{\tau \in \Omega_h} h_\tau$ is a measure of the granularity of the triangulation Ω_h; and P_1 is the space of linear polynomials.

A second discrete space is defined as

$$H_{h_g}^1 = \left\{ q_h \,|\, q_h \in H_h^1,\ q_h|_\Gamma = g \right\}, \tag{11}$$

where Γ indicates the boundary of the domain and g the value that the function q_h assumes along this boundary.

In words, H_h^1 represents the ensemble of the continuous polynomials, defined over the discretized domain, and $H_{h_g}^1$ the sub-ensemble of the polynomials belonging to H_h^1 that satisfy given boundary conditions.

The discrete variational formulation corresponding to eqn (2) can be expressed as follows:

Find $\psi_l \in H_{h_g}^1$

such that:

$$\sum_{\tau \in T} \frac{1}{K} \int_\tau \nabla \psi_l \cdot \nabla v\ \mathrm{d}\tau = 0 \quad \forall v \in H_{h_0}^1 \tag{12}$$

The contribution to the global integral coming from each triangle τ in the triangulation T, is given by

$$\mathbf{A}_\tau \psi_{l_\tau} = 0, \tag{13}$$

where $\mathbf{A}_\tau$ is a 3×3 symmetric and positive definite matrix associated with the element τ, and ψ_{l_τ} is a 3×1 vector corresponding to the three vertices of τ. Thus, the assembly of all contributions of elementwise matrices and right-hand-sides leads to the following global matrix equation:

$$\mathbf{A}\psi_l = 0. \tag{14}$$

Here, $\mathbf{A}$ is an $NV \times NV$ symmetric and positive definite matrix (NV is the total number of nodes on the mesh), while ψ_l is an $NV \times 1$ vector containing the value of the streamfunction at all triangulation nodes.

The system (14) has a unique solution, and the classical conjugate gradient algorithm can be applied to solve this system (see, for example, Ref.[30] for details). We also use the "mass lumping" technique as preconditioner[31] which accelerates the convergence of the conjugate gradient algorithm.

4 *A POSTERIORI* ERROR ESTIMATE

The *a posteriori* error estimate approach was introduced by Babuška for general problems[32]; results of theoretical research on *a posteriori* error estimates for elliptic equations can be found also in Refs.[33,34]. Here, we will adapt these results to the problem of computing the streamfunction (the same procedure being followed with the potential).

Consider that the piecewise linear solution, $\psi_l \in H^1_{h_g}$, is now available satisfying

$$\sum_{\tau\in T}\frac{1}{K}\int_\tau \nabla\psi_l\cdot\nabla v\,\mathrm{d}\tau = 0 \quad \forall v\in H^1_{h_0}. \tag{15}$$

We define the error as

$$e = \psi - \psi_l, \tag{16}$$

Since we solve the streamfunction problem using linear elements, the local approximation of e should be given in terms of at least piecewise quadratic finite element basis functions. We will use here the discrete space B_τ, defined over each triangle τ and consisting of a set of quadratic polynomials vanishing at each one of the three vertices.

Inspired by the approach of Bank[33], we obtain using Green's formula from eqn (1) the following local (within each τ) Neumann problem:

Find $e_\tau \in B_\tau$

such that:

$$\int_\tau \nabla e_\tau\cdot\nabla w\,\mathrm{d}\tau = -\int_\tau \nabla\psi_{l,\tau}\cdot\nabla w\,\mathrm{d}\tau + \int_{\partial\tau}\frac{1}{2}\left(\frac{\partial}{\partial n}(\psi_{l,\tau}+\psi_{l,\text{neighbor}})+\frac{\partial}{\partial n}(e_\tau+e_{\text{neighbor}})\right)w\,\mathrm{d}s \quad \forall w\in B_\tau, \tag{17}$$

where the index 'neighbor' denotes all the triangles surrounding the triangle τ (see Fig. 2).

Obviously, the above equation cannot be solved because it contains the unknown term $\int_{\partial\tau}\frac{1}{2}\frac{\partial}{\partial n}(e_\tau + e_{\text{neighbor}})w\,\mathrm{d}s$ on the right-hand side. We drop this term and reduce eqn (17) into the following *a posteriori* error *estimate* criterion:

Find $\tilde{e}_\tau \in B_\tau$

such that:

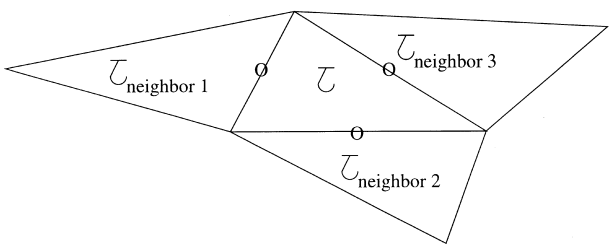

Fig. 2. τ and its three neighbors.

$$\int_\tau \nabla\tilde{e}_\tau\cdot\nabla w\,\mathrm{d}\tau = -\int_\tau \nabla\psi_{l,\tau}\cdot\nabla w\,\mathrm{d}\tau + \int_{\partial\tau}\frac{1}{2}\frac{\partial}{\partial n}(\psi_{l,\tau}+\psi_{l,\text{neighbor}})w\,\mathrm{d}s \quad \forall w\in B_\tau \tag{18}$$

This is a local Neumann problem, involving the error estimate at the middle point of the three edges of the triangle τ. Thus, for each triangle τ, the system (18) leads to a 3×3 matrix equation. Since the matrix resulting from $\int_\tau \nabla\tilde{e}_\tau\cdot\nabla w\,\mathrm{d}\tau$ is symmetric and positive definite, the uniqueness of the solution is ensured. Note that the hydraulic conductivity coefficient, K, does not appear in eqns (17) and (18) because in this study K is constant within each triangle τ.

The *a posteriori* error estimate can be used to compute both local and global "*energy norms*" as follows:

$$|||\tilde{e}|||_\tau^2 = \frac{1}{K}\int_\tau \nabla\tilde{e}_\tau\cdot\nabla\tilde{e}_\tau\,\mathrm{d}\tau \tag{19}$$

$$|||\tilde{e}|||_T^2 = \sum_{\tau\in T}\frac{1}{K}\int_\tau \nabla\tilde{e}_\tau\cdot\nabla\tilde{e}_\tau\,\mathrm{d}\tau. \tag{20}$$

The local energy norm (19) serves as error index for each triangle τ, suggesting whether to modify τ. In fact, Bank[33] has mathematically proved that, measured by the above energy norms (19) and (20), the actual error e (defined by eqn (16)) and the *a posteriori* error estimate $\tilde{e}$ (resulting from solving eqn (18)) are equivalent. Guided by this index, we can approximately equi-distribute the error over the mesh through simultaneous refinement/unrefinement operations; finally, we can make this uniformly distributed error value as small as required through further refinement sweeps. The overall quality of each mesh can be measured by the global energy norm of the error eqn (20).

5 ADAPTIVE MESH PROCEDURES

Based on the *a posteriori* error estimate, we adapt the mesh through bisection refinements, unrefinements, edge swaps, and node moving. These mesh adaptation procedures produce a triangulation on which granularity varies gradually, improving its geometric quality and reducing the error related to the discretization.

For illustration, consider that triangle τ_1 in Fig. 3(a) is selected for refinement because it has the biggest local energy norm of the error expressed by eqn (19). The τ_1 triangle is bisected by the median line to its longest edge. This refinement procedure, originally suggested by Rivara[28], is called *longest-edge bisection*. Following this bisection, we should also refine τ_2, the triangle sharing the bisected edge with τ_1. If the bisected edge happens to be the longest edge in τ_2, the local refinement process can stop. In our example, the refinement of τ_2 that is shown in Fig. 3(b) violates the longest-edge bisection rule, since the common edge of τ_1 and τ_2 is not the longest one in the triangle τ_2.

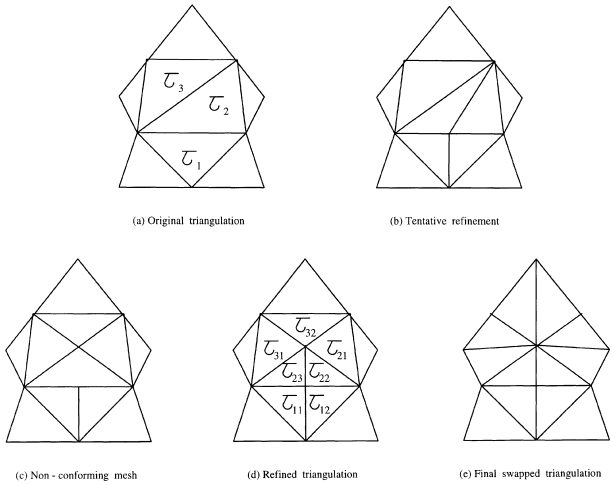

Fig. 3. Refinement example.

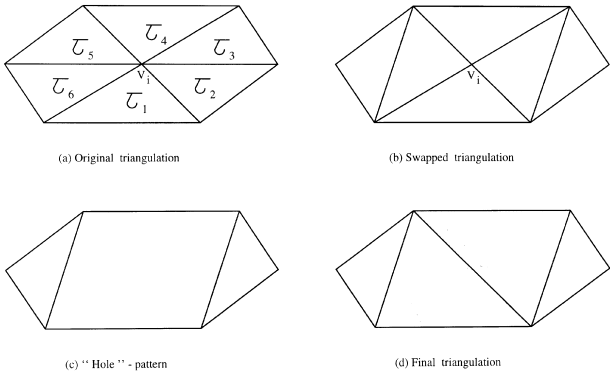

Fig. 4. Unrefinement example.

We recursively refine elements, i.e., we will continue to bisect the longest edge of each triangle until the common edge of two neighboring elements to be refined is the longest for both. This process typically consists of a few steps. In our case, it just takes two steps, resulting in the triangulation shown in Fig. 3(c), which is unfortunately non-conforming. We supplement refinements, producing τ_{22} and τ_{23} in Fig. 3(d), to make the triangulation conforming as shown in Fig. 3(d).

The mesh quality of the refined triangulation, shown in Fig. 3(d), can be further improved by local edge swaps. We implement edge-swap loops only for newly-refined elements. That is, we identify its longest edge and the neighboring element that shares this edge; using criteria such as the geometric quality of the involved triangles or, again, the *a posteriori* error estimate, we compare the existing pattern and another pattern with common edge swapped, and we select the better pattern. Through local edge swaps, the final triangulation, shown in Fig. 3(e), looks nicer than the one presented in Fig. 3(d).

Note that the geometric quality of a triangle τ is quantified using the metric $4\sqrt{3}|\tau|/\sum_{i=1,3} h_i^2$, where $|\tau|$ and $h_i (i = 1, 3)$ are the area and the three sides of the triangle τ; this quality index reaches 1, its maximum value, when τ is an equilateral triangle.

In this work, we coarsen the mesh by deleting nodes located in regions characterized by the smallest errors. At first, we transform the elementwise constant error estimate distribution into a new distribution, in which the error estimate is distributed among nodes. This transformation is achieved by assigning to each vertex the average of the errors of the surrounding triangles. Then, we start our unrefinement process from the vertices with the smallest error indices.

For example, in Fig. 4(a), we have selected to eliminate node v_i. First, we reduce the surrounding triangles number from six to four, by successively swapping edges among the existing six elements. Unrefinement is guided preferably by the criterion of geometric quality; it yields an intermediate swapped triangulation as shown in Fig. 4(b). In this case, we can remove the node v_i, obtaining a quadrilateral "hole"-pattern as illustrated in Fig. 4(c). To divide the quadrilateral hole, making a conforming triangulation, we have two possible connecting choices; obviously, the subdivision shown in Fig. 4(d) is more acceptable based on *a priori* geometric criterion.

Our mesh moving algorithm can be guided by either geometric quality or *a posteriori* error estimate criterion, although in a slightly different fashion. In this algorithm, the mesh connectivity remains fixed, but the locations of mesh points can be changed to satisfy requirements of geometric quality or error estimate. Our procedure consists of a Gauss–Seidel-like iteration on the vertices of the mesh, in which the position of each vertex is locally optimized with all the other vertices kept fixed. The procedure is illustrated in Fig. 5, where the position of the vertex v_i is optimized within the region Ω_{v_i} by the approximate optimization of the geometric quality or the approximate minimization of the *a posteriori* error estimate as function of the vertex location. Each optimization problem has two degrees of freedom, and it is solved using a simple approximate Newton iteration scheme. Details about this algorithm can be found in Ref.[35]. Notice that not all the vertices in the mesh can be moved. Some boundary and interface vertices must remain fixed to preserve the definition of the region; other vertices are characterized by only one degree of freedom.

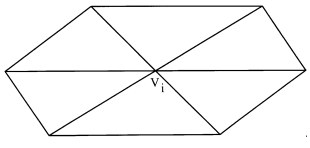

Fig. 5. The subregion Ω_{vi} associated with vertex v_i.

6 NUMERICAL EXPERIMENT

We present the numerical simulation of groundwater flow in a 1 m × 1 m square domain. The logarithm of conductivity (i.e., the logarithm of the hydraulic conductivity) is a sample from a random function that is stationary and normally distributed with Gaussian covariance function:

$$R(h_x, h_y) = \sigma^2 \sqrt{\left(\frac{h_x}{l_x}\right)^2 + \left(\frac{h_y}{l_y}\right)^2}, \tag{21}$$

where R is the covariance at distance h_x in the horizontal direction and h_y in the vertical direction. The conductivity is measured in units of m/s. The mean of logarithm of conductivity is -9.21, the variance σ^2 is 2, and the length parameters l_x and l_y are 0.1 and 0.01 m, respectively. The sample was generated using a procedure developed by Dykaar *et al.*[36–40]. We generate a hydraulic conductivity background over a 3 m × 3 m square domain, which is represented by 1025 × 1025 points (that is, the length, 3 m, and the height, 3 m, are divided into 2^{10} units, respectively); then, we retain the central 1 m × 1 m subdomain which is one-ninth of the total area. The resulting hydraulic conductivity field is thus periodicity-free. The sample hydraulic conductivity has $\ln(K_{\max}) = -4.046$ and $\ln(K_{\min}) = -14.04$.

At first, we generated a regular coarse triangulation on which the unit length is 0.05 m in the x and y directions. The conductivity, shown in Fig. 6, has $\ln(K_{\max} = -5.404$ and $\ln(K_{\min}) = -13.13$. The computed streamlines are shown in Fig. 7 and the *a posterior* error estimates for the streamfunction are shown in Fig. 8, indicating that the initial mesh is inadequate.

Then, based on the *a posteriori* error estimate, we successively add points, setting the target number of nodes, NV_{target}, first at 1000 and then at 2000. The two refined meshes have 1000 nodes and 1916 elements (Fig. 9) and 2000 nodes and 3865 elements (Fig. 10), respectively. We emphasize that, on these adapted meshes, the grid is highly nonuniform in node density, with higher density in higher conductivity areas.

Fig. 11 shows the mesh resulting from a further mesh improvement, realized through simultaneous refinements/unrefinements, with $NV_{\text{target}} = 3000$. Points located in lower conductivity regions are progressively deleted, while the node density in higher conductivity areas increases further. This grid, characterized by 3000 nodes and 5857 elements, has no similarity to the original uniform mesh. The channeling of flow in preferential flow paths illustrated on Fig. 12 is much more pronounced than computed in the original coarse uniform grid (see Fig. 7).

However, some streamlines appear rippled. Also, note that the maximum hydraulic conductivity value captured by this third adapted mesh is $\ln(K_{\max} = -4.056$ (see Fig. 13) while we are expecting it to reach -4.046. By refining the grid even further, the accuracy of the computed streamlines can be improved even further. The operation of simultaneous refinement/unrefinement is carried out once more, yielding the mesh with 4000 nodes and 7848 triangles as shown in Fig. 14. Another further mesh refinement produces a grid con-

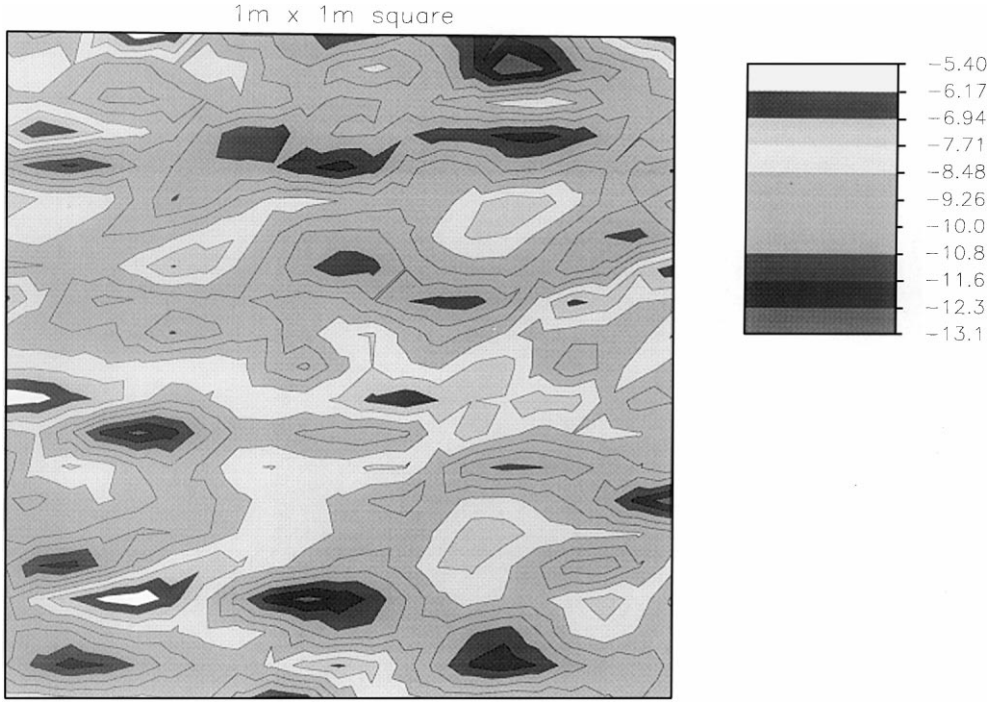

Fig. 6. ln(K) associated with initial mesh.

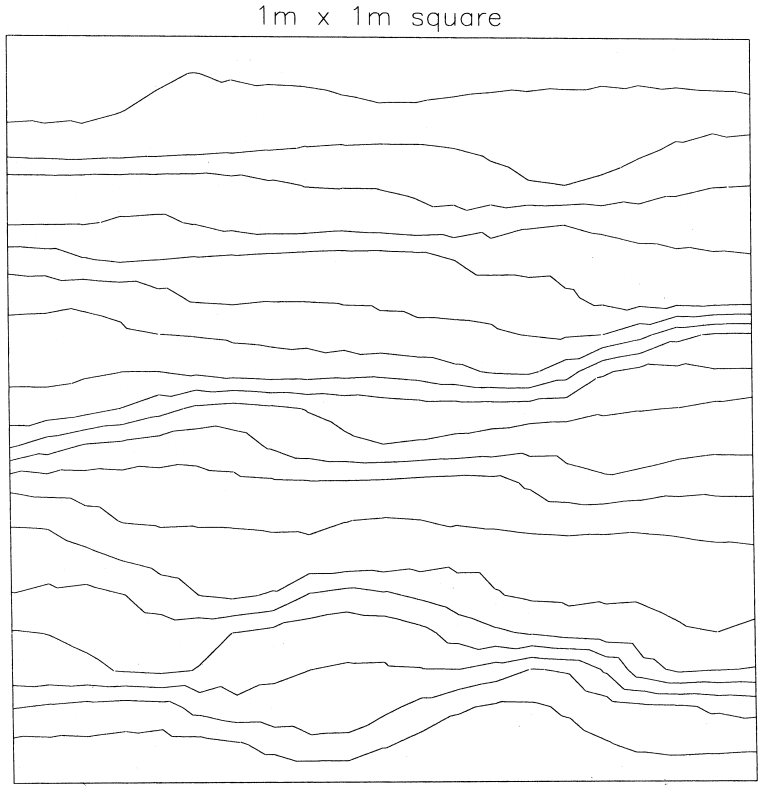

Fig. 7. Streamlines associated with the initial mesh (the discharge passing between two consecutive plotted streamlines is 0.05 if the total discharge is regarded as 1).

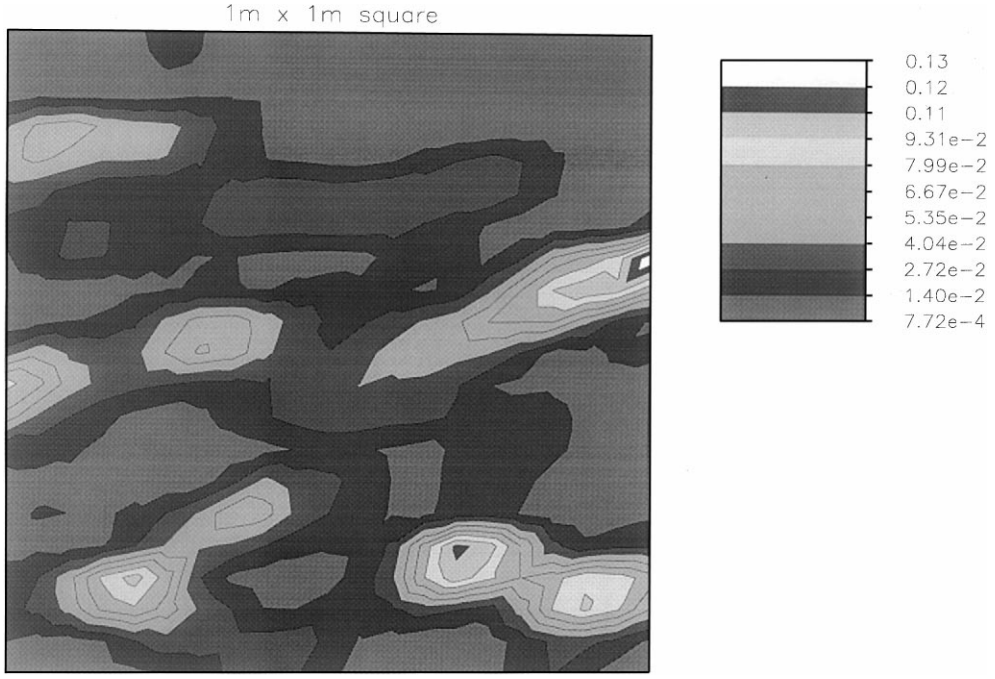

Fig. 8. Local error "energy norm" distribution associated with initial mesh.

taining 5000 points and 9845 elements (see Fig. 15). We use this latest mesh as final adapted grid, because the maximum expected hydraulic conductivity values: $\ln(K_{\max}) = -4.046$, is captured (see Fig. 16). The most striking feature of this mesh is that most nodes are concentrated in the high hydraulic conductivity regions

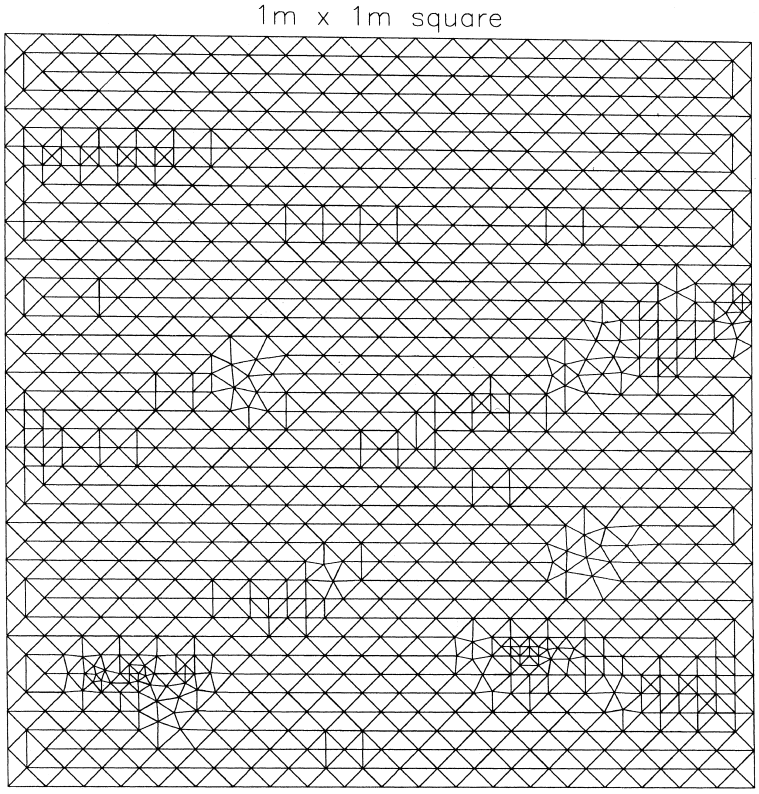

Fig. 9. The first adapted mesh ($NV = 1000$, $NT = 1916$).

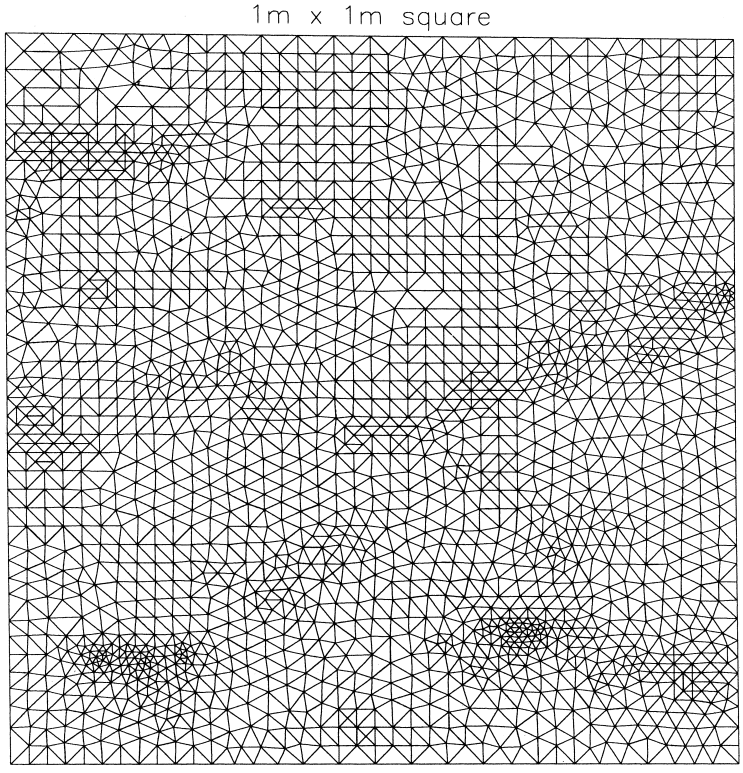

Fig. 10. The second adapted mesh ($NV = 2000$, $NT = 3865$).

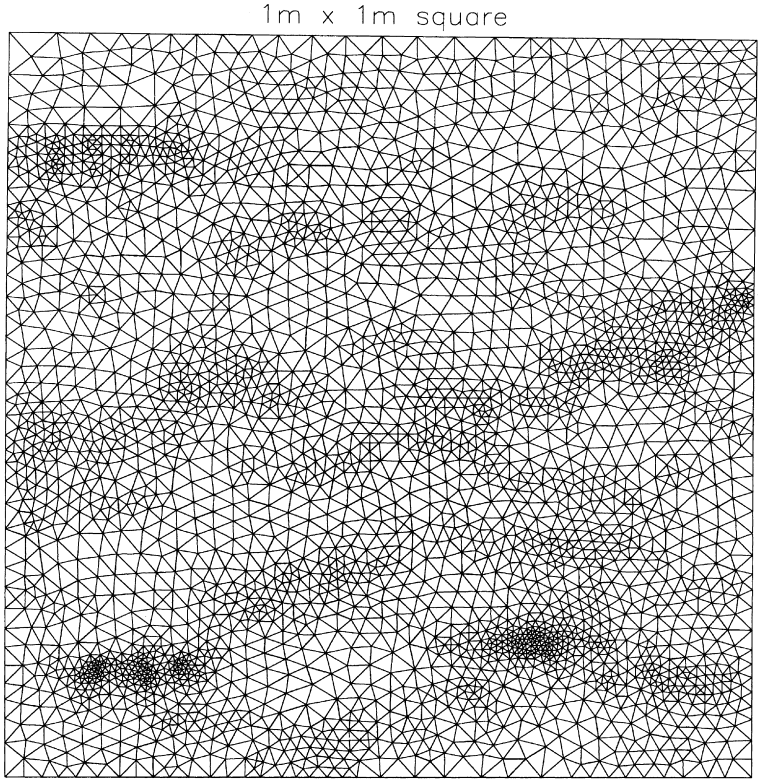

Fig. 11. The third adapted mesh ($NV = 3000$, $NT = 5857$).

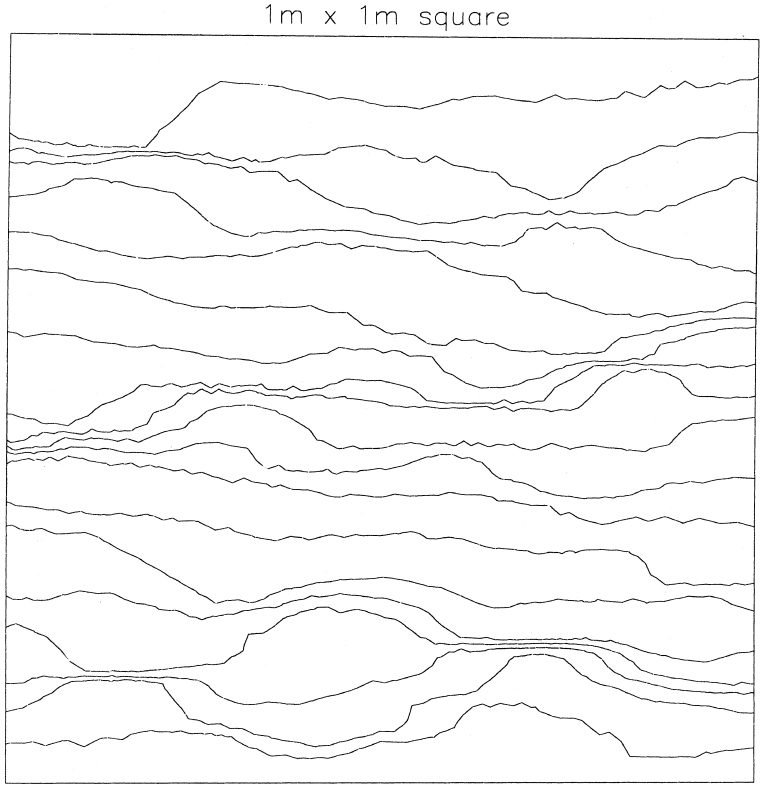

Fig. 12. Streamlines associated with the third adapted mesh (the discharge passing between two consecutive plotted streamlines is 0.05 if the total discharge is regarded as 1).

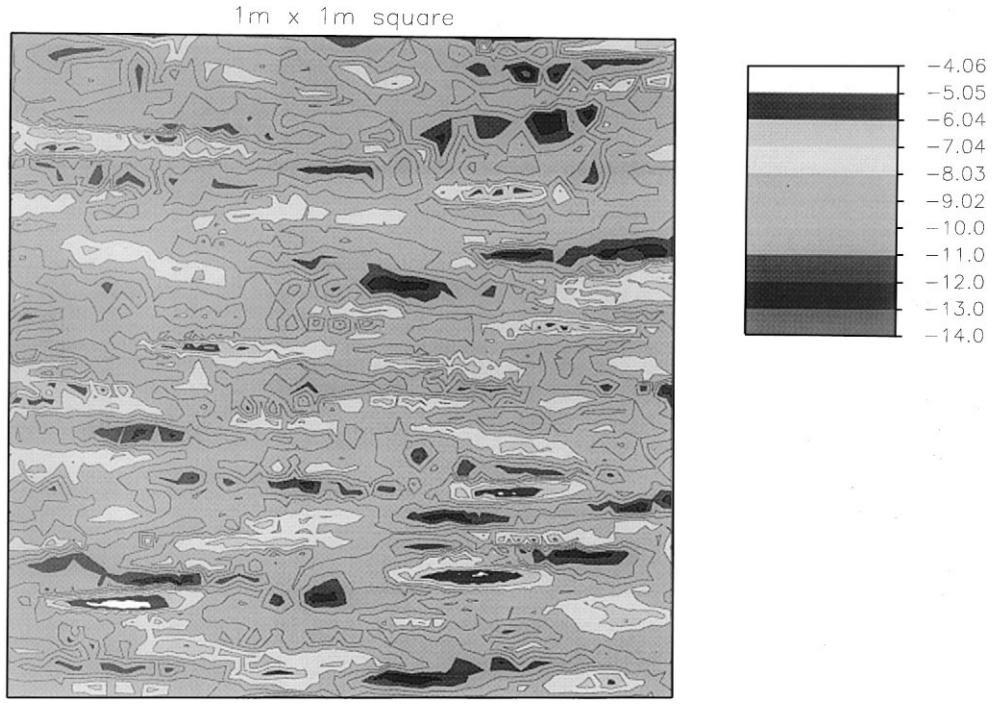

Fig. 13. ln(K) associated with the third adapted mesh.

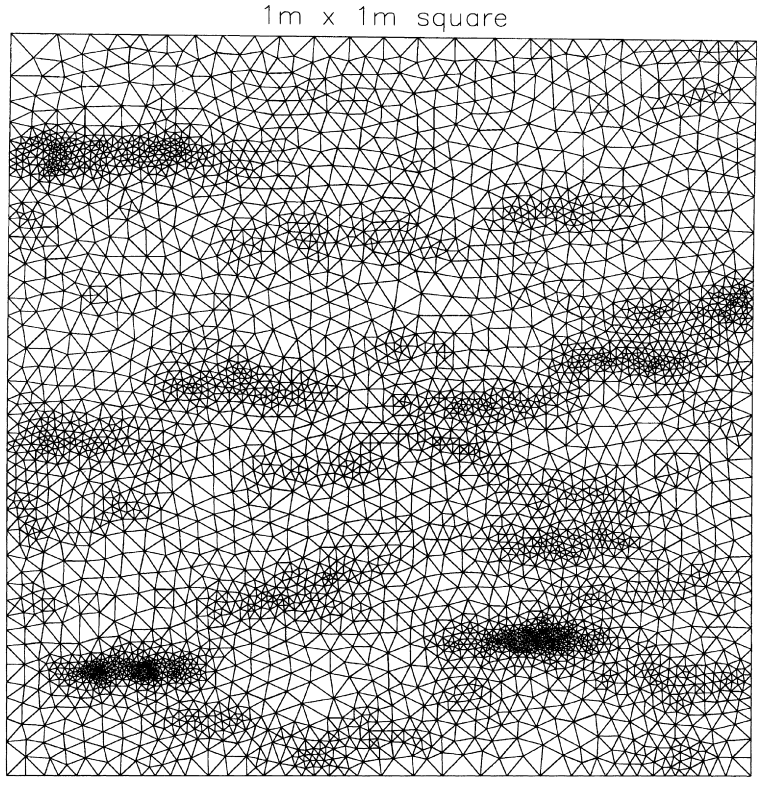

Fig. 14. The fourth adapted mesh ($NV = 4000$, $NT = 7848$).

where the flow rate is the highest. Fig. 17 shows the flownet associated with the fifth adaptive grid. On this mesh, the channeling of streamline pattern is even more pronounced while the smoothness of streamlines in these sensitive areas looks better than in Fig. 12 characterized by 3000 nodes; meanwhile, the orthogonality of streamlines to equipotential lines is ensured in this numerical experiment. The associated *a posteriori* error

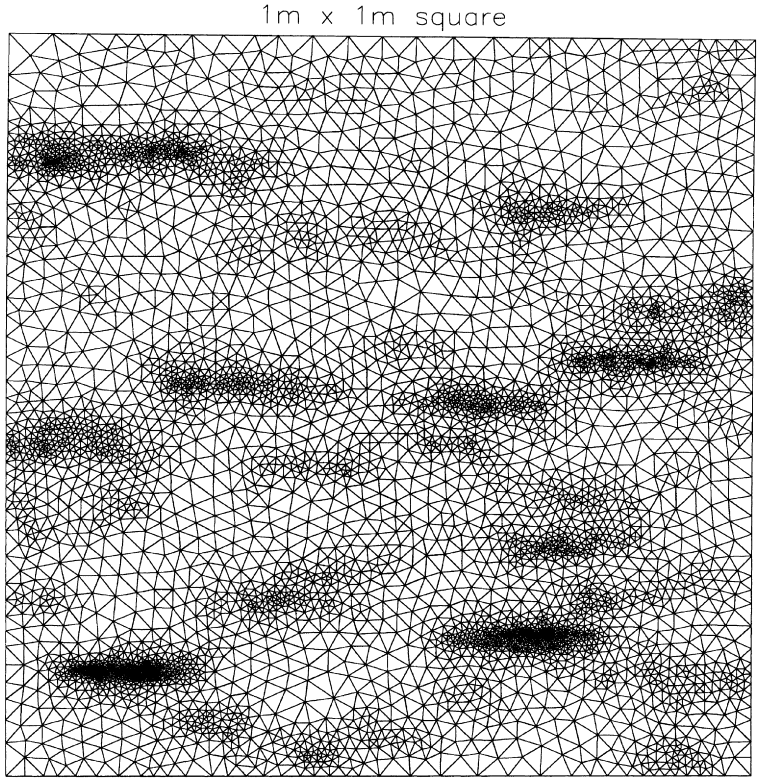

Fig. 15. The fifth adapted mesh ($NV = 5000$, $NT = 9845$).

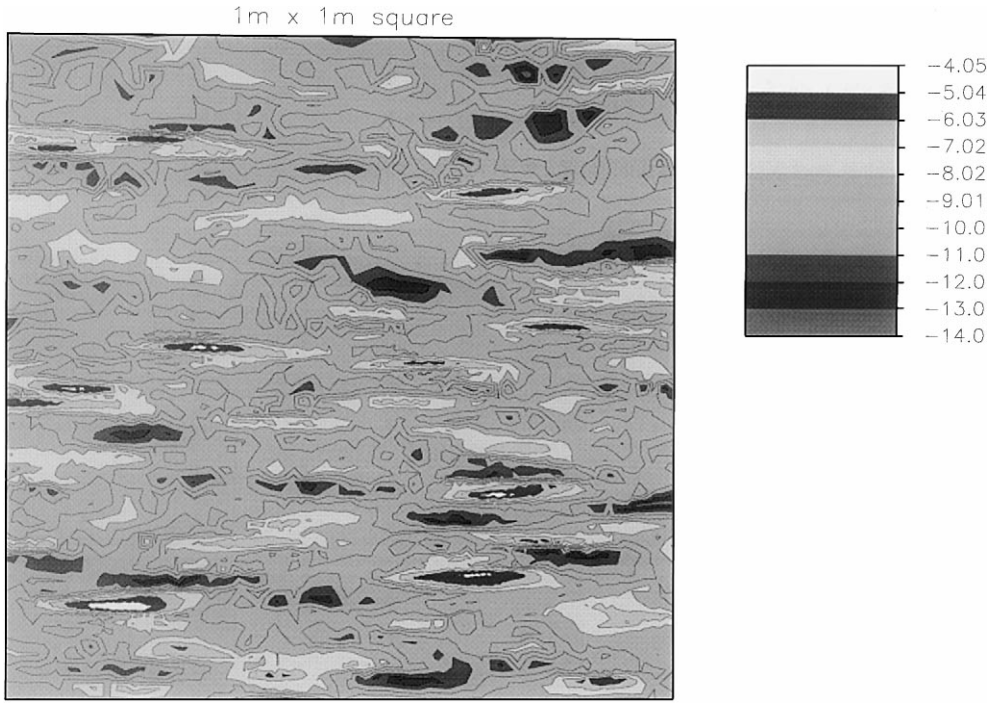

Fig. 16. $\ln(K)$ associated with the fifth adapted mesh.

estimate distribution, illustrated in Fig. 18, is almost six orders of magnitude smaller than the original one.

We also analyzed the results to look for the relationship between the density of nodes and the value of the mean specific discharge module (see eqn (5) for the definition of the specific discharge vector). We divide the 1 m × 1 m square into 100 0.1 m × 0.1 m subsquares, calculating the mean specific discharge module value of

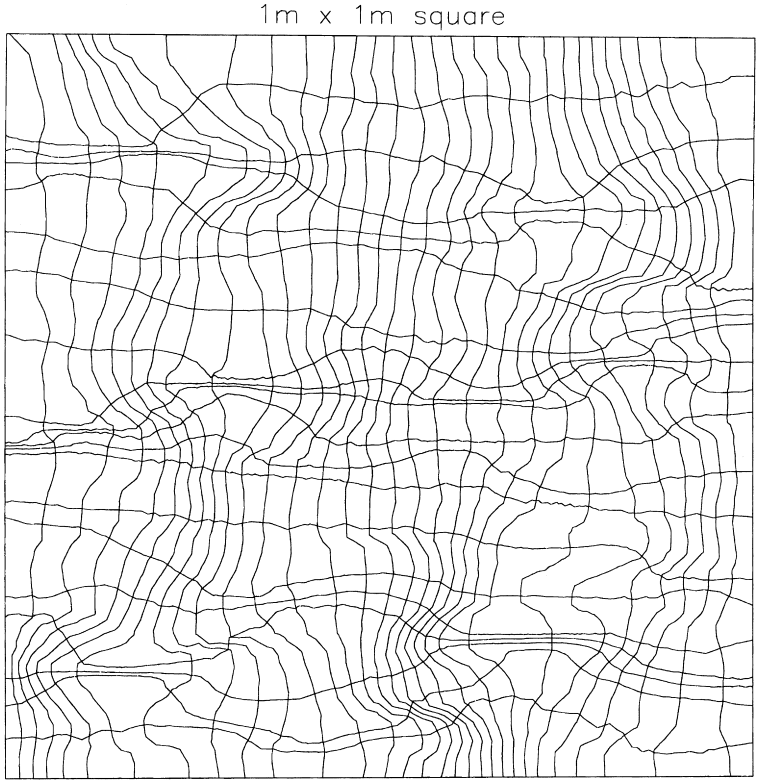

Fig. 17. Flownet associated with the fifth adapted mesh (the discharge passing between two consecutive plotted streamlines is 0.05 if the total discharge is regarded as 1).

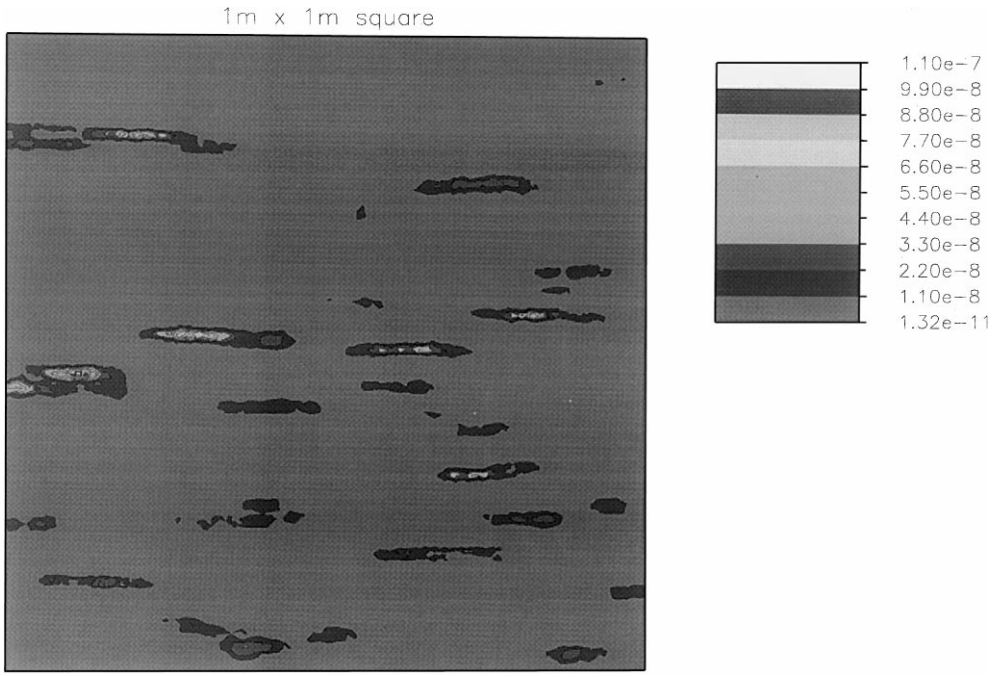

Fig. 18. Local error "energy norm" distribution associated with the fifth adapted mesh.

each block and counting the number of nodes occupied in the block. The resulting 100 sampled data are plotted in Fig. 19. The figure shows clearly that lower velocities are found in a larger part of the area and a bigger node density is essential to describe the zones with higher velocities. In Fig. 20, we have plotted $|(K_{\max})_{\text{num}} - (K_{\max})_{\text{actual}}|/(K_{\max})_{\text{actual}} \times 100\%$ as a function of the number of nodes. As we can see, the more adapted the

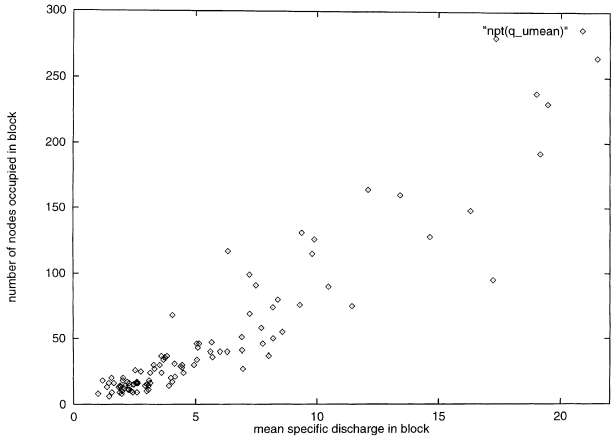

Fig. 19. Relationship between specific discharge module mean value distribution and node number distribution on the fifth adapted mesh (statistics on 100 equally-divided squares of 0.1 m × 0.1 m).

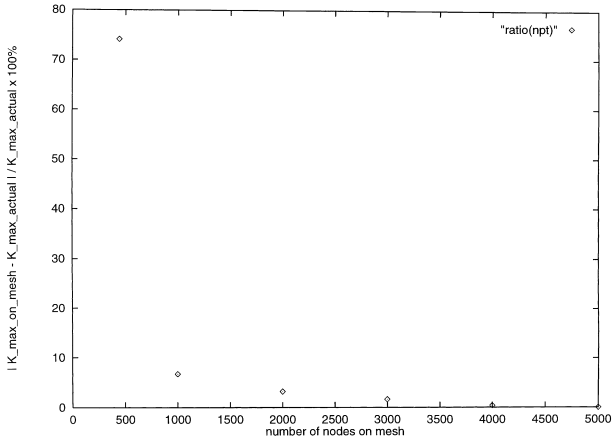

Fig. 20. Evolution of efficiency of $K_{\max}$-capturing during successive mesh adaptations.

mesh, the closer the maximum conductivity value is to the theoretical one, showing that finer meshes tend to resolve better the actual maximum hydraulic conductivity of the formation.

In the present work, every refinement/unrefinement process is followed by a node-moving adjustment that improves the mesh quality. Also, note that the solution of eqns (1) and (2) is required whenever a new adaptive mesh is generated, because our *a posteriori* error estimate is computed on the basis of the updated finite element solution.

For comparison purposes, we have additionally generated a very fine uniform mesh on which the unit length is 0.01 m in both x and y directions. This fine reference grid uses 10 201 nodes and 20 000 elements. The corresponding finite element solution for the streamfunction is shown in Fig. 21. Although the grid is quite fine, it is not sufficient to resolve the high conductivity areas (the maximum triangle conductivity is only $\ln(K_{\max}) = -4.11$). More importantly, the degree of channeling is underestimated and the streamlines are more uniformly distributed than those on the adaptively selected nonuniform grid with almost half the number of nodes. The *a posteriori* error estimate distribution associated with this reference mesh is illustrated in Fig. 22, indicating the poor error-reducing ability of such a uniform fine mesh though twice more nodes are used compared to our final adapted mesh.

7 CONCLUDING REMARKS

The accurate simulation of flow is an integral part of the successful simulation of solute transport in heterogeneous formations. Of course, the accurate representation of flow is a multifaceted problem involving site characterization, proper scaling, and numerical analysis. This work focuses on numerical modeling, especially the choice of a proper finite-element grid. In heterogeneous formations, the streamlines computed through a coarse regular grid may be significantly off. For example, compare the streamlines in Fig. 7 with the streamlines computed using a much finer regular grid with 10 201 nodes (Fig. 21) or an adaptively designed nonuniform grid with only 5000 nodes (Fig. 17). The streamlines from the coarse grid tend to miss the channeling of flow in preferential flow paths. The difficulty with fine meshes is the high computational cost, which generally increases faster than the square of the number of nodes.

Finite element mesh adaptivity guided by *a posteriori* error estimate analysis can enhance the accuracy of numerical groundwater-flow simulation with moderate increase in cost. Nodes are distributed unevenly, so that the density is higher where needed. The final adaptive grid reflects the contrasts in the conductivity distribution. Node density is generally higher in areas with larger hydraulic conductivity and faster flow. Mesh adaptation is carried out automatically.

Even though a certain number of mesh adaptive processes are involved in the computation, the CPU percentage used for the grid optimization remains less than 20%. Compared with the uniform fine-grid mesh employed for comparison purposes in this work, the total CPU time associated with our adaptive procedure is just about 15% longer. That is, the total CPU time for the adaptively computed streamlines in Fig. 17 is about the same with the total CPU time for the streamlines of the regular fine-grid mesh in Fig. 21. However, the result of the adaptive approach describes the groundwater flow definitely better.

The methodology presented in this paper can be extended to three-dimensional simulation. The *a posteriori* error estimate analysis applies in the three-dimensional case as it applies in two-dimensional flow. However, the three-dimensional finite element mesh adaptation would be a new algorithmic development. Compared to two-dimensional mesh adaptive algorithm, the adjacent

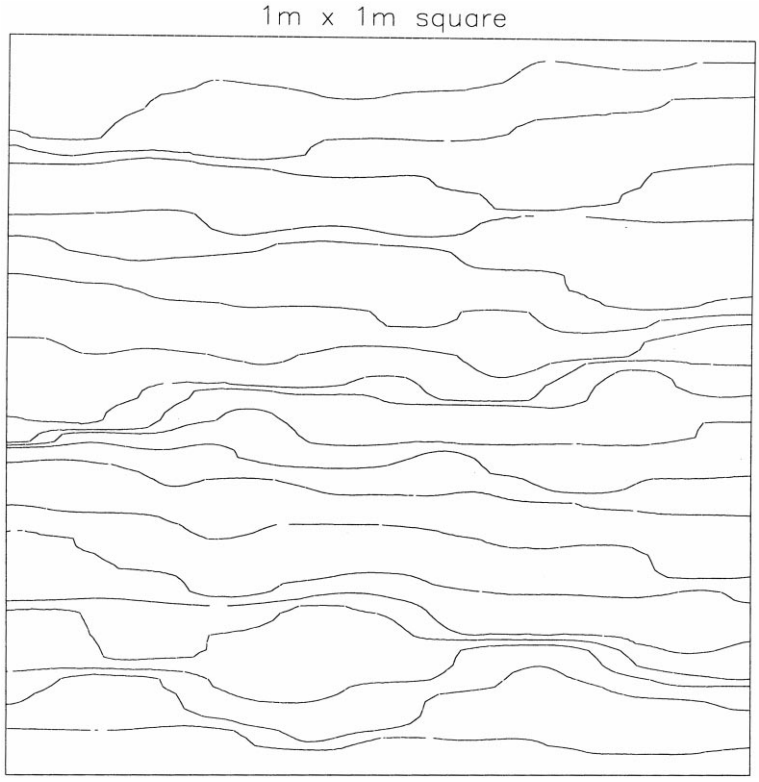

Fig. 21. Streamlines associated with the reference mesh (the discharge passing between two consecutive plotted streamlines is 0.05 if the total discharge is regarded as 1).

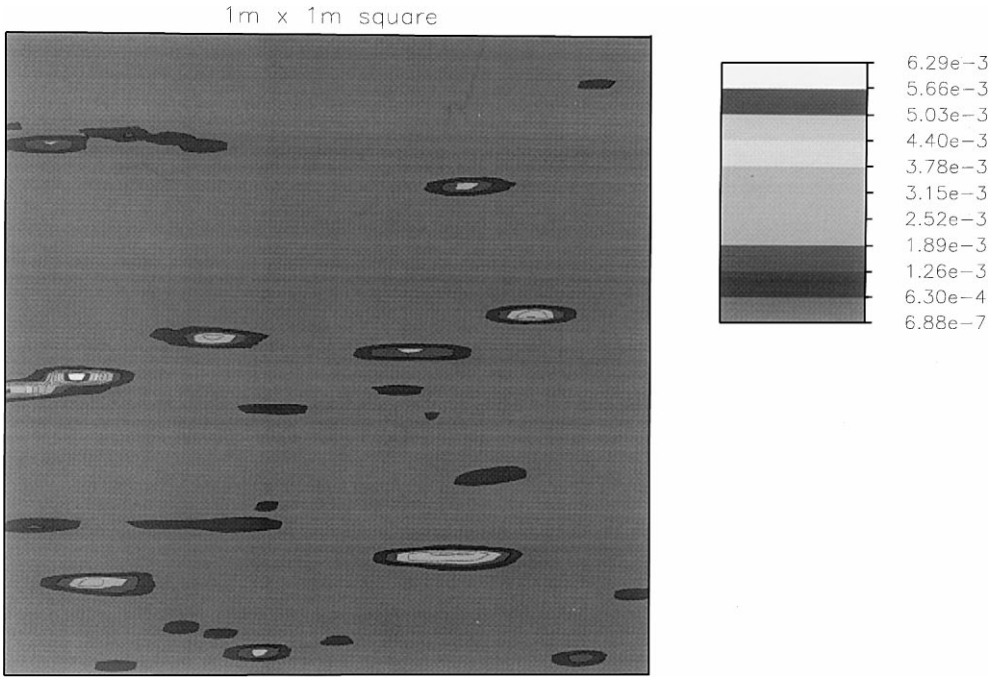

Fig. 22. Local error "energy norm" distribution associated with the reference mesh.

elements (for example, tetrahedrons) share not only sides but also faces, which requires additional data structures to record the enriched relationships between neighboring three-dimensional finite-elements. Although the code that combines three-dimensional finite-element mesh adaptation with *a posteriori* error esti-

mator could be more complicated than the current two-dimensional model, the extension of the approach to three-dimensional analysis is promising.

ACKNOWLEDGEMENTS

This work was supported with funding from the National Science Foundation under project EAR-9523922, "Constitutive Relations of Solute Transport and Transformation" and EAR-9522651, "Factors Controlling Solute Dilution in Heterogeneous Formation"; and Dupont, through project LBIO-71113. We also would like to thank Professor R.E. Bank at the Department of Mathematics in the University of California, San Diego, for his software PLTMG that serves partially as a basis of our work.

REFERENCES

1. Pinder, G. and Gray, W., *Finite Element Simulation in Surface and Sub-surface Hydrology*, Academic Press, New York, 1977, p. 295 .
2. Huyakorn, P.S. and Pinder, G.F., *Computational Methods in Subsurface Flow*, Academic Press, New York, 1983.
3. Frind, E.O. and Matanga, G.B., The dual formulation of flow for contaminant plumes with large dispersive contrast: Evaluation of alternating direction Galerkin techniques. *Water Resour. Res*., 1985, **21**, 159–169.
4. Kinzelbach, W., *Groundwater Modelling*, Elsevier, Amsterdam, 1986, p. 333.
5. Bear, J. and Verruijt, A., *Modeling Groundwater Flow and Pollution with Computer Programs*, Reidel, Dordrecht, 1987, p. 414.
6. Celia, M.A. and Gray, W.G., *Numerical Methods for Differential Equations*, Prentice-Hall, 1992.
7. Cordes, C. and Kinzelbach, W., Continuous groundwater velocity fields and pathlines in linear, bilinear and trilinear finite elements. *Water Resour. Res*., 1992, **28**, 2903–2911.
8. Cordes, C. and Kinzelbach, W., Comment on "Application of the mixed hybrid finite element approximation in a groundwater model: Luxury or necessity?" by Mosé, R., Siegel, P., Ackerer, P. and G. Chavent. *Water Resour. Res*., 1996, **32**, 1905–1909.
9. Barry, D.A., Bajracharya, K. and Miller, C.T., Alternative split-operator approach for solving chemical reaction/groundwater transport models. *Advances in Water Resources*, 1996, **19**(5), 261–275.
10. Cao, J. and Kitanidis, P.K., Adaptive finite element simulation of Stokes flow in porous media. *Advances in Water Resources*, 1998, **22**(1), 17–31.
11. Moreno, L. and Tsang, C., Flow channeling in strongly heterogeneous porous media. *Water Resour. Res*., 1994, **30**(5), 1421–1430.
12. Borcea, L. and Papanicolaou, G., A hybrid numerical method for high contrast conductivity problems. *Journal of Computational and Applied Mathematics*, 1997, **87**, 61–77.
13. Borcea, L. and Papanicolaou, G., Network approximation for transport properties of high contrast materials. *SIAM Journal on Applied Mathematics*, to appear.
14. Ames, W.F., *Numerical Methods for Partial Differential Equations*, Academic Press, San Diego, CA, 1992.
15. Chavent, G. and Roberts, J.E., A unified physical presentation of mixed, mixed-hybrid finite elements and standard finite difference approximations for the determination of velocities in waterflow problems. *Advances in Water Resources*, 1992, **14**, 329–348.
16. Brezzi, F. and Fortin, M., *Mixed and Hybrid Finite Element Method*, Springer, New York, 1994.
17. Durlofsky, L.J., Accuracy of mixed and control volume finite element approximations to Darcy velocity and related quantities. *Water Resour. Res*., 1994, **30**(4), 965–973.
18. Mosé, R., Siegel, P., Ackerer, P. and Chavent, G., Application of the mixed hybrid finite element approximation in a groundwater model: Luxury or necessity? *Water Resour. Res*., 1994, **30**, 3001–3012.
19. Frind, E.O., Sudicky, E.A. and Schellenberg, S.L., Micro-scale modelling in the study of plume evolution in heterogeneous media. *Stochastic Hydrol. Hydraul*., 1987, **1**, 263–279.
20. Cirpka, O., Frind, E. and Helmig, R., Streamline oriented grid generation for transport modelling in two-dimensional domains including wells, *Advances in Water Resources*, 1999, **22**(7), 697–710.
21. Cirpka, O., Frind, E. and Helmig, R., Numerical simulation of biodegradation controlled by transverse mixing, submitted to *J. Contam. Hydrol*., submitted.
22. Cao, J. and Kitanidis, P.K., An algorithm for solving reactive advection-dispersion problems, Tech. Report, Stanford University, 1997.
23. Babuška, I., Zienkiewicz, O.C., Gago, J. and de A. Oliveira, E.R., Accuracy estimates and adaptive refinements in finite element computations. In *Accuracy Estimates and Adaptivity in Finite Element Computations*, eds. I. Babuška, O.C. Zienkiewicz and E.R.A. Oliveira, Wiley, New York, 1986.
24. Demkowicz, L., Oden, J.T. and Rachowicz, W., A new finite element method for solving compressible Navier–Stokes equations based on an operator splitting method and *h–p* adaptivity. *Computer Methods in Applied Mathematics and Engineering*, 1990, **84**, 275–326.
25. Bank, R.E., *PLTMG: A Software Package for Solving Elliptic Partial Differential Equations,* Users' Guide 6.0., Frontiers in Applied Mathematics, SIAM, Philadelphia, 1990.
26. George, P.L., Hecht, F. and Saltel, E., Automatic mesh generator with specified boundary. *Computer Methods in Applied Mathematics and Engineering*, 1991, **92**, 269–288.
27. Barry J., GEOMPACK – a software package for the generation of meshes using geometric algorithms. *Adv. Eng. Software*, 1991, **13**(5/6), 325–331.
28. Rivara, M.C., Algorithms for refining triangular grids suitable for adaptive and multigrid techniques. *J. Numer. Meth. Engrg*., 1984, **20**, 745–756.
29. Kitanidis, P.K., Groundwater flow in heterogeneous formations. In *Sub-surface Flow and Transport: The Stochastic Approach*, eds. G. Dagan and S.P. Neuman, Cambridge Univ. Press, 1997, pp. 83–91.
30. Glowinski, R., *Numerical Methods for Nonlinear Variational Problems*, Springer, New York, 1984.
31. Pironneau, O., *Finite Element Methods for Fluids*, Masson, Paris, 1989.
32. Babuška, I. and Rheinboldt, W.C., *A posteriori* error estimates for the finite elements method. *Int. J. Numer. Methods Eng.*, 1978, **12**, 1597–1615.
33. Bank, R.E., Analysis of a local *a posteriori* error estimator for elliptic equations. In *Accuracy Estimates and Adaptivity in Finite Element Computations*, eds. I. Babuška, O.C.

Zienkiewicz and E.R.A. Oliveira, Wiley, New York, 1986, pp. 119–128.
34. Babuška, I., Strouboulis, T. and Upadhyay, C.S., A model study of the quality of a posteriori error estimators for linear elliptic problems. *Comput. Methods Appl. Mech. Engrg.*, 1994, **114**, 307–378.
35. Bank, R.E. and Smith, R.K., Mesh smoothing using *a posteriori* error estimates. *SIAM J. Numerical Analysis*, 1997, **34**, 979–997.
36. Dykaar, B.B., Program documentation for the two- and three-dimensional codes used to compute: random fields, effective flow parameters, specific discharges, covariances, and cross-covariances, and display the results, 1994, Tech. Report, Stanford University.
37. Lent, T.V., Numerical Spectral methods applied to flow in highly heterogeneous aquifers, Ph.D. Thesis, Stanford University, 1992.
38. Dykaar, B.B. and Kitanidis, P.K., Determination of the effective hydraulic conductivity for heterogeneous porous media using a numerical spectral approach, 1: Method. *Water Resour. Res.*, 1992, **28**(4), 1155–1166.
39. Dykaar, B.B. and Kitanidis, P.K., Determination of the effective hydraulic conductivity for heterogeneous porous media using a numerical spectral approach, 2: Results. *Water Resour. Res.*, 1992, **28**(4), 1167–1178.
40. Dykaar, B.B. and Kitanidis, P.K., Transmissivity of a heterogeneous formation. *Water Resour. Res.*, 1993, **29**(4), 985–1001.